



Dealing with plasmonic crystal biosensors: Sensitivity assessment of nanodisks/nanoholes arrayed plasmonic system for label-free DNA detection

Daiki Kawasaki ^a, Ryosuke Nishitsuji ^b, Tatsuro Endo ^{c,*}

^a Metamaterials Laboratory, RIKEN Cluster for Pioneering Research, 2-1 Hirosawa, Wako, 351-0198, Saitama, Japan

^b Department of Information Networking, Graduate School of Information Science and Technology, Osaka University, 2-8 Yamadaoka, Suita, Osaka, 565-0871, Japan

^c Department of Applied Chemistry, Graduate School of Engineering, Osaka Metropolitan University, Sakai, 599-8531, Japan

ARTICLE INFO

Keywords:

Plasmonic crystal
Label-free biosensor
DNA sensing
Plasmonic biosensor
Gold nanostructure

ABSTRACT

Label-free optical deoxyribonucleic acid (DNA) sensing with arrayed plasmonic nanostructures (plasmonic crystals) is a promising technology for biomedical diagnosis and bioanalytical science. Plasmonic biosensors can detect target biomolecules by utilizing the shift in plasmonic resonance caused by changes in the surrounding refractive index (RI) attributed to the capture of target biomolecules using a recognizer. Conventional explanations for the sensitivity of plasmonic crystals are based on bulk (BRIS) and surface RI sensitivities (SRIS) for basic plasmonic nanoparticles despite their unique properties such as surface lattice resonances (SLRs), wherein localized surface plasmons (LSPs) cooperatively oscillate with their pitch. Therefore, investigating the sensitivity of SLRs is imperative for improving sensing performance. In this study, the sensitivity of adenomatous polyposis coli (APC) gene-related DNA hybridization detection of complementary plasmonic crystals composed of nanodisks (PNDs) on or under plasmonic nanoholes (PNHs) was investigated considering the SLR properties. The BRIS was measured using the conventional definition of the peak wavelength shift per unit RI increment (nm/RIU) followed by the SRIS measurement using the layer-by-layer method. The BRIS and SRIS measurements reflect the practical sensitivity for DNA detection. PNHs had higher sensitivity than PNDs, with a limit of detection of 0.30 nM. Further, only the SLR-based mode responded to localized RI changes because of DNA hybridization, whereas both the LSPs- and SLR-based modes responded to uniform RI changes caused by layer-by-layer coating. Our investigation will open up possibilities and opportunities for plasmonic crystal biosensors.

1. Introduction

Label-free biosensing using plasmonic nanostructures is a promising approach to detect and observe biomarkers such as deoxyribonucleic acid (DNA), proteins, and extracellular vesicles with high sensitivity and via simple operations (Altug et al., 2022; Anker et al., 2008; Bonyár, 2020; Sadighbayan et al., 2020; Shrivastav et al., 2021). Plasmonic label-free sensors can optically detect biomolecules by utilizing the response of plasmonic resonance to physical or chemical changes in the surrounding medium of the nanostructure covered by a plasmonically enhanced electromagnetic (EM) field. The sensitivity and accuracy of plasmonic biosensors depends on the uniformity and intensity of its enhanced EM field distribution because the spatial overlaps and light-matter interactions between enhanced EM fields and target

molecules determine responsivity (Chung et al., 2011; Feuz et al., 2010; Jatschka et al., 2016). Thus, the shape and arrangement of plasmonic structures can affect sensing capability because plasmonic-enhanced EM field distributions are characterized by these structural characteristics (Kawasaki et al., 2019a; Willets and Duyne, 2007). Bottom-up-based nanostructures enable low-cost fabrication and wide availability; however, their sensitivity and accuracy remain relatively low owing to the uniformity or low intensity of the enhanced EM field caused by the limitations in engineering their shape and the randomness in structural arrangement. Top-down fabricated nanostructures incur high costs and limit availability because of their need for nanofabrication facilities; however, periodically arrayed, geometrically designed structures can offer a strong and uniformly enhanced EM field to realize high sensitivity and accuracy (Altug et al., 2022; Kim et al., 2007; Szunerits and

* Corresponding author.

E-mail address: t_endo@omu.ac.jp (T. Endo).

Boukherroub, 2012; Tang and Li, 2017; Guo et al., 2015; Kawasaki et al., 2019a; Luo et al., 2019; Sreekanth et al., 2016). Plasmonic crystals can create highly uniformly enhanced EM fields that expand on the surface based on surface lattice resonances (SLRs), collectively coupled to localized surface plasmons (LSPs) (Kravets et al., 2018). Plasmonic crystal sensors have been applied successfully not only in scientific research but also in practical medical diagnostics because of these excellent plasmonic features (Ansaryan et al., 2023; Belushkin et al., 2020; Li et al., 2017). Further, plasmonic crystal sensors can be mass produced using the nanoimprinting technique, which is widely used in the medical and industrial fields (Kawasaki et al., 2019a, 2019b; Luo et al., 2019; Nishiguchi et al., 2016). Therefore, understanding and developing plasmonic crystal sensors can contribute to advances in biosensing technologies and medical diagnoses.

Plasmonic sensors utilize the shift in the resonance peak caused by changes in the refractive index (RI) of the effective surrounding medium. Bulk RI sensitivity (BRIS) is a conventional indicator used to evaluate sensitivity and is defined as the ratio of the wavelength shift to the change in the RI of the bulk solution (Chung et al., 2011; Willets and Duyne, 2007). However, this indicator cannot adequately represent sensitivity for biomolecule detection. The effective responsive area is directly related to the plasmonically enhanced EM field, which decays exponentially from the nanostructured surface to the bulk area. Some studies successfully demonstrated the effective surface RI sensitivity (SRIS) of plasmonic sensors by evaluating their responsivity to the surrounding polymer layers or protein bilayers (Li et al., 2022; Zhan et al., 2020), which prove that the sensitivity of plasmonic sensors correlates with their plasmonic-enhanced EM field. Although the explanation for the sensitivity of plasmonic crystal sensors is based on the nanoparticle-based LSP response theory; plasmonic crystals have unique properties characterized by their array system. In contrast to the localized surface plasmon resonance (LSPR) generated on the surface of a closed nanostructure, SLR is characterized by its dispersion relationship, i.e., the plasmonic band. The conventional response and the plasmonic band shift in detecting biomolecules should be investigated to reveal the sensitivity of plasmonic crystals for biosensing.

The sensitivity of the plasmonic crystal sensor was investigated using the BRIS, SRIS, and label-free detection of DNA hybridization with the adenomatous polyposis coli (APC) gene sequence, which is related to the regulation of important events in cell growth and cancer cells (Esteller et al., 2001; Ge et al., 2012). Our plasmonic crystal sensor comprises a periodic array of nanodisks and holes that are efficiently mass produced by nanoimprinting techniques, thereby enabling high-throughput investigations of biosensing applications (Endo et al., 2010, 2012; Kawasaki et al., 2022). Further, the concavo-convex structure, i.e., the nanodisks on or under the hole plates, can be reversed during the fabrication stage. In this paper, the former and the latter are referred to as plasmonic nanodisks (PNDs) and plasmonic nanoholes (PNHs), respectively. The PNDs and PNHs are characterized experimentally and numerically using microspectroscopic measurements and finite-difference time-domain (FDTD) calculations. Further, the BRISs of the PNDs and PNHs are evaluated by measuring the plasmonic peak shift corresponding to the bulk RI change in a sucrose solution, which is a well-known conventional method. After BRIS measurements, the SRISs of plasmonic crystals were evaluated under air and water conditions using a layer-by-layer (LbL) method, which enables coating a monolayer polymer with a thickness of a few nanometers on a nanostructure surface (Feldötö et al., 2010; Ray et al., 2007). The sensitivity of the DNA hybridization detection was evaluated experimentally to demonstrate plasmonic DNA sensing. Finally, the plasmonic band shift caused by ds-DNA binding to the plasmonic crystal surfaces was observed for evaluating how the SLRs properties contributed to the response for DNA detection. Comparing the plasmonic band shifts caused by DNA hybridization with those caused by LbL coating revealed that spectral responses were different between the uniform and localized RI changes.

2. Materials and methods

2.1. Fabrication of plasmonic crystals

A cycloolefin polymer (COP)-based hole-array structured film developed in a previous study was used as the mold for nanoimprint lithography (Fig. S1). First, the COP mold was cleaned with 2-propanol (Kanto Chemical Co. Inc., Tokyo, Japan) and ultrapure water and dried at room temperature (20–25 °C). Subsequently, an Au layer (thickness: $t = 50, 100, \text{ and } 150 \text{ nm}$) was deposited thermally onto the COP mold. This Au hole-array nanostructure was used as PNHs. PNDs were prepared by attaching the deposited Au layer to a glass substrate using a UV-curable polymer (NOA81, Norland Products Inc., Cranbury, USA), followed by the dissolution of the COP mold in limonene (Kanto Chemical Co. Inc., Tokyo, Japan). The nanostructures were observed using field-emission scanning electron microscopy (FE-SEM) (SU8010, Hitachi, Ibaraki, Japan) at an acceleration voltage of 10 keV.

2.2. Optical characterization

The experimental optical characterization of the plasmonic crystals was performed by measuring the refraction spectra using our homemade spectroscopic setup (Fig. S2a). Plasmonic bands were observed using a homemade 0–20° reflectoscopic setup (Fig. S2b), and the optical properties of the plasmonic crystals were characterized by numerical calculations using the FDTD method (FDTD-solution, Ansys, Inc., Vancouver, Canada). A plane wave was used as the light source, electric field profiles and reflection intensity were calculated by field monitors, periodic boundary conditions were set in the x-y direction, and a perfect matching layer was set in the z direction. In the oblique-angle incidence, bfast was set in the plane wave.

2.3. BRIS and SRIS measurements

A 0–30 wt% aqueous sucrose solutions (Wako Pure Chem. Co., Osaka, Japan) were used for the BRIS measurements. BRIS is defined as the ratio of the shift in the peak wavelength to the change in the RI of the solutions: $\text{BRIS} = \Delta\lambda_{\text{peak}}/\Delta n$ (nm/RIU). SRIS is evaluated using the LbL method, wherein aqueous solutions of poly (allylamine hydrochloride) (PAH) and poly (sodium 4-styrenesulfonate) (PSS; 3 mg/ml) containing 0.5M NaCl are used. A bilayer of the PAH and PSS monolayers is defined as one layer in this study. Plasmonic crystals were immersed in the PAH solution for 1 min, followed by rinsing with ultrapure water. After rinsing, the surfaces were dried using an air blower. Next, the plasmonic crystals with the PAH layer were immersed in the PSS solution for 1 min, followed by rinsing with ultrapure water. The lamination process was repeated an arbitrary number of times. The thickness of each layer was ~2 nm (Fig. S3), and the RI of the LbL bilayer was considered as 1.5 [30]. PAH and PAH were purchased from Sigma-Aldrich Japan Co., LLC (Tokyo, Japan), and NaCl was purchased from Kanto Chemical Co. Inc. (Tokyo, Japan).

2.4. Label-free detection of DNA hybridization

The oligonucleotides used in the present study were purchased from BEX Co. Ltd. (Toyota, Japan). 5' disulfide-modified 40 base pair (bp) long sequence probe and fully complimentary target DNA were used in the present study (see Table S1). The present sequence is related to the APC gene. A phosphate-buffered saline (PBS) solution (pH 7.4) purchased from Wako Pure Chem. Co. (Osaka, Japan) was used for immobilizing the thiolated probe on the Au surface and hybridizing the target DNA. The thiolate probe DNA (1 μM in buffer) was immobilized on the surface of the plasmonic crystals by incubating at 37 °C overnight, followed by rinsing with ultrapure water to remove non-specifically adsorbed DNA and a buffer solution. A complimentary target DNA (1 nM–1 μM in buffer) was hybridized by incubating at 37 °C for 1 h and

rinsed with a PBS buffer for 5 min. The peak shifts for each DNA sample were analyzed in air and under PBS. Optical measurements of all DNA samples were performed in triplicate using three independent samples ($N = 3$).

3. Results

3.1. Optical characterization of the plasmonic crystals

The PNDs and PNHs were fabricated using nanoimprinting techniques (Fig. S1). Schematic and SEM images of the PNDs and PNHs are shown in Fig. 1a-d. The thickness of the Au layer was 100 nm, the diameters of the PND nanodisks and the holes of the PNHs were 220 nm, and the pitch of both crystals was 440 nm. These plasmonic crystals were fabricated from the same mold, and therefore, the PNDs and PNHs were complementary. The experimental and simulated reflection spectra of the PNDs and PNHs in air and water conditions are shown in Fig. 1e-h. The incident light was polarized along the x-direction. Two peaks (i and ii) observed in the experimental spectra of PNDs and PNHs under each condition well agreed with the simulated spectra, and subsequently, their enhanced electric field distributions were characterized based on the simulation (Fig. 1i-l). In air, the enhanced electric fields at the peak wavelength were distributed around the top of the nanodisks/nanoholes of the PNDs and PNHs, whereas those at the peak ii wavelength were distributed over the entire surface because of the plasmonic coupling between the nanodisks and nanoholes. In water, both electric fields at peaks i and ii wavelengths were distributed over the entire surface. The plasmonic couplings at the peak i wavelength were in the anti-binding mode, and those at the peak ii wavelength were in the binding mode (Fig. S4). For PNDs, both peaks were observed in the experimental spectra, whereas for PNHs, peak ii was barely observed. The bonding mode of peak ii of the PNDs is more observable than that of the PNHs because the nanostructured surface of the latter is composed of nanodisks “on” the nanoholes plate, which increase the coupling efficiency of the disk-hole coupling mode to incidental light, whereas the

PNHs nanostructured surface composed of nanodisks “under” nanohole plate decrease the coupling efficiency. It seems that more peaks are observed in the simulated spectra than the experimental spectra, but actually the broaden peak in experimental spectra contained several peaks which could be observed in the simulation. In addition, the peak wavelength in water red-shifted form that in air because of increase in surrounding RI from 1 to 1.333. The wavelength shift in PNHs were higher than that in PNDs due to higher RI sensitivity of PNHs than that of PNDs, which is discussed in the next section.

The enhanced electric field distribution reflects the area where the plasmonic mode responds to the surrounding medium; however, the enhanced electric field distribution is not directly correlated to sensitivity, which is expressed by a plasmonic mode shift that corresponds to the change in the surrounding medium because the sensitivity depends not only on the distribution of the enhanced electric field, but also on the shape of the nanostructured surface, which generates an enhanced electric field.

3.2. BRIS and SRIS of the plasmonic crystals

The BRIS of the PNDs and PNHs were measured considering the shift in the peak wavelength shift corresponding to the change in the bulk RI, $\text{BRIS} = \Delta\lambda_{\text{peak}}/\Delta n$ (nm/RIU), using the sucrose aqueous solution. Fig. 2a and b show the reflection spectra of the PNDs and PNHs in each solution with different RI values. The peak wavelength red shifted with increasing RI. The BRISs of mode i and ii of the PNDs were 127.6 and 142.0 nm/RIU, respectively. In addition, the peak wavelength shift of mode i was not sufficiently linear to calculate BRIS ($R^2 = 0.947$) (Fig. S5a). Mode ii of the PNDs was evaluated in the following experiments. The BRISs of peaks i and ii of PNHs were 447.8 and 101.4 nm/RIU, respectively (Fig. S5b). Peak ii was not distinguished from peak i in the bare experimental spectra of PNHs, and therefore, both peaks were analyzed using Lorentzian fitting. The BRIS of mode ii was lower than that of mode i because of the disturbance in the disk-hole bonded coupling caused by the experimental nonuniform nanostructure. In the

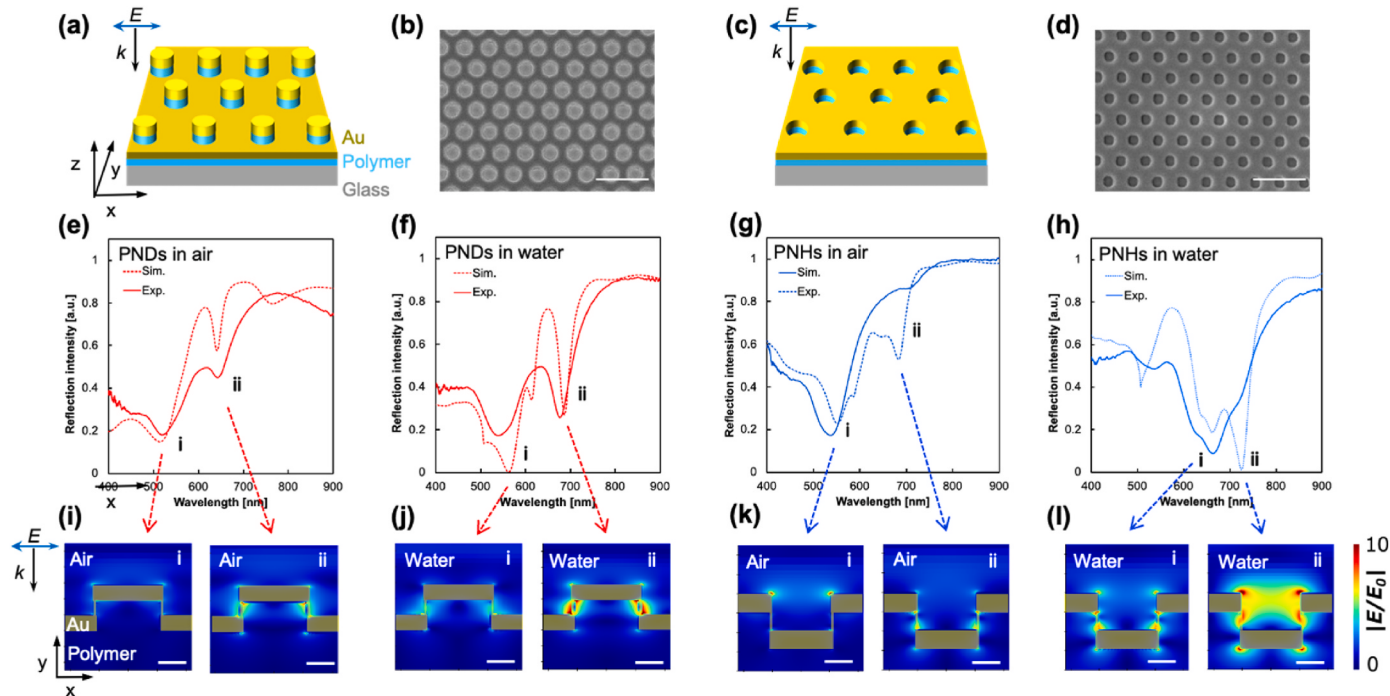


Fig. 1. Characterization of PNDs and PNHs. a, c) Schematics of the PNDs and PNHs. b, d) SEM images of PNDs and PNHs surface (x-y plane). Scale bars indicate 500 nm. e-h) Reflection spectra of PNDs and PNHs under air or water conditions. The solid lines represent an experimental spectrum, and the dashed lines represent the calculated spectrum. i-l) Electric field distributions at the peak wavelength (i and ii). The incident polarization was along the x-direction. The intensity is described by $|E/E_0|$, where E_0 represents the electric field of incidence. The scale bars represent 100 nm.

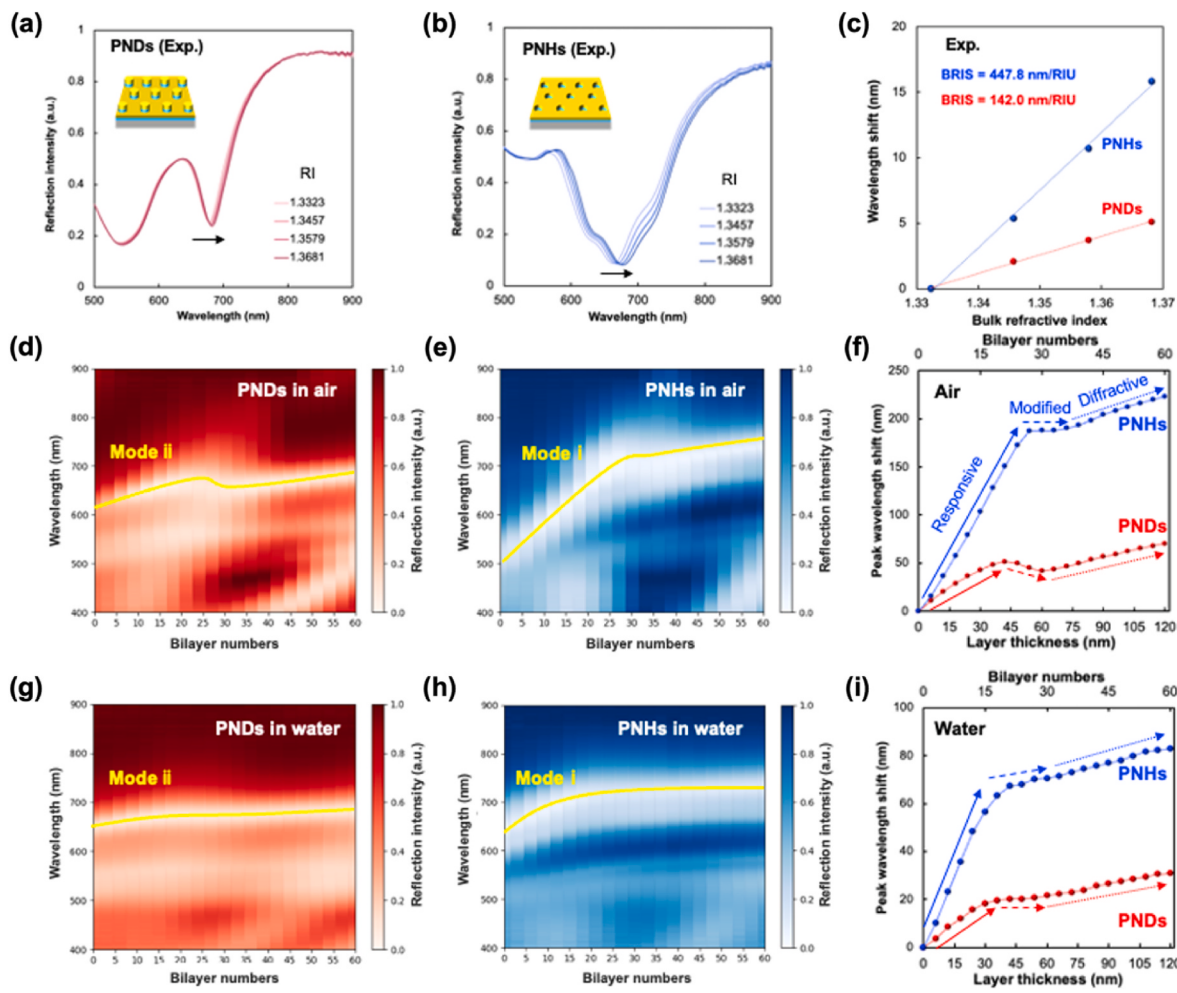


Fig. 2. Evaluation of BRIS and SRIS of PNDs and PNHs. a, b) Reflection spectra of PNDs (a) and PNHs (b) in sucrose aqueous solutions with various RI. The peaks to be evaluated were indicated by black arrows. c) The plots of peak wavelength shifts of PNDs (Red) and PNHs (Blue) corresponding to each RI of the solutions. The shift value was calculated by the difference in the peak wavelength from water to each sucrose solutions (10, 20, and 30 wt%). The BRISs of PNDs and PNHs were shown by the corresponding color. d, e) The reflection spectra of PNDs (d) and PNHs (e) with each number of bilayers under the air condition. The reflection intensity is represented by the color scale. The yellow solid line indicates the shift of mode ii of PNDs and mode i of PNHs. f) The plots of the peak shift of PNDs (Red circle) and PNHs (Blue circle) corresponding to the number of bilayers. The upper x-axis shows the number of bilayers and the lower x-axis shows the approximate thickness, which is derived by 2 nm per bilayer. g-h) Reflection spectra of PNDs (d) and PNHs (e) with each numbers of bilayers under the water condition, and the plots of the peak shift of PNDs (Red circle) and PNHs (Blue circle).

following experiments, peak i of PNHs was evaluated because it was experimentally observable and had a higher sensitivity than that of peak ii. Fig. 2c represents the peak wavelength shift to the RI of the solution. Next, the SRISs of PNDs and PNHs were evaluated using the LbL method, via which the nanostructure surface was covered with a few nanometers thick polycations and polyanions attributed to the electrostatic self-organization. In our experiment, the thickness of the bilayer composed of PAH and PSS was ~2 nm, which was analyzed by observing the surface of the PNDs with 0–30 bilayers (Fig. S6). The LbL coating on the plasmonic crystals was performed on up to 60 bilayers, and the maximum thickness of the coated polymer bilayers was ~120 nm. The thickness of the dielectric medium was expected to be sufficient for saturating the plasmonic response. The RI of the bilayers was considered as 1.5 in the experiment. Fig. 2d and e shows the reflection spectra of PNDs and PNHs under air conditions corresponding to each bilayer number from 0 to 60; the reflection dips are indicated by white lines. In Fig. 2d, modes i and ii of the PNDs are indicated by yellow solid and dashed lines, respectively, whereas in Fig. 2e, mode i is indicated by the yellow solid line. Fig. 2f shows the reflection peak shifts attributed to mode i of the PNDs and mode ii of the PNHs with an increase in the number of bilayers and corresponding approximate thickness. The

plasmonic response to the increase in polymer thickness was observed to stop at ~40 nm in the PNDs plots and 60 nm in the PNHs plots, where the region was indicated as a responsive area. After the responsive area, the peak did not shift in the range of 60–75 nm in the PNHs plots. In contrast, the peak was blue shifted by 45–60 nm in the PNDs plots. These regions were indicated as modified areas, wherein the thickness range of the plasmonic modes of the PNDs and PNHs was reconfigured by forming a symmetric RI-matching condition between the polymers under the substrate and top media. Further, after the modified region, moderate red shifts were observed in both the PNDs and PNHs plots, which could be attributed to the diffractive shift caused by an increase in the bulk polymer thickness. This diffraction shift could be partially caused by the numerical apertures of the objective lens in the optical measurements. The results under the water conditions are shown in Fig. 2g-i. The saturated peak shifts of both PNDs and PNHs were ~2.5 times lower than those under air conditions, which could be attributed to the smaller RI difference between the LbL polymer and bulk condition. These results reflect the effective responsivity to surface RI changes, which reveal that the sensitivity of the PNHs was higher than that of the PNDs. To analyze the SRIS of PNDs and PNHs, the plots were fitted by plasmonic responsive curves expressed by

$$\Delta\lambda = s \times (n_{poly} - n_{bg}) \times \left(1 - e^{-\frac{2t}{l_d}}\right) \quad (1)$$

where $\Delta\lambda$ and s represent the peak-shift and sensitivity factor, respectively, and n_{poly} and n_{bg} represent the RI of the polymers and background medium, respectively. The fitting parameters are listed in Table S2 and the fitting method is explained in Text S1. t and l_d represent the thickness of the LbL polymer and the effective decay length of the plasmonic mode, respectively. In the case of PNDs under the air condition, s and l_d were 120.6 nm/RIU and 51.1 nm, whereas in the case of PNHs, these factors were 423.0 nm/RIU and 75.3 nm. Under the water condition, s and l_d of PNDs were 136.8 nm/RIU and 43.3 nm, while these factors of PNHs were 437.3 nm/RIU and 44.4 nm. The PNDs and PNHs exhibited similar values under both air and water conditions, moreover the BRISs of both plasmonic crystals reflect sensitivity factors. In contrast, the effective decay length l_d in water was shorter than that in air for both PNDs and PNHs. The second-order partial derivative of $\Delta\lambda$ was calculated based on the factors derived in eq. (1) to evaluate the SRISs in more detail (Text S2, Fig. S7). The second-order SRISs on the surface ($t = 0$ nm) of the PNDs and PNHs in water were higher than those in air, which could be related to the shorter effective decay length l_d in water than that in air. This suggests that the sensitivity to unit RI changes on the surface of the plasmonic crystals in water are higher than those in air, which can be attributed to the enhanced electric field generated by each mode, as shown in Fig. 1i–l. However, the second-order SRIS represents the sensitivity to a unit RI change on the surface, i.e., the responsivity to the difference in RI between the coated layer on the surface and the initial bulk medium. Thus, the second-order SRIS does not work as an indicator of sensitivity to some RI change under every condition; however, it does so when compared under the same conditions. In practical sensing

applications to detect biomolecules within a medium that is a few tens of nanometers thick, the slope of the responsive area works as an indicator of sensitivity. Slopes in the responsive regions of the PNDs and PNHs under air and water conditions were analyzed, as indicated in Fig. S8. The slopes of PNDs and PNHs in air were 3.11 and 1.65 under the air condition, and 1.95 and 0.67 under the water condition. The PNHs showed a higher sensitivity than that of the PNDs in terms of both the BRIS and SRIS. Thus far, the sensitivity to uniform RI change in bulk for BRIS and on the surface for SRIS has been evaluated; however, the localized RI change is induced in practical biosensing applications, including the detection of DNA hybridization.

3.3. Sensitivity for label-free DNA hybridization detection

The sensitivity of plasmonic crystals for detecting DNA hybridization was evaluated. We evaluated the sensing performance of plasmonic crystals to develop a highly sensitive sensor for label-free analysis of the APC sequence. The methylated APC sequence has recently gained attention in the medical science field because extraordinary methylation in the APC sequence is considered to be correlated with some types of cancers. The DNA sequence used in the experiments was composed of 40 bp, which had a molecular length of ~13.6 nm. Fig. 3a and b show the reflection spectra of the PNHs before and after probe DNAs (1 μm) immobilize onto the surface and after hybridization with the target DNAs (1 μm), respectively. A red shift in the peak wavelength was observed for each probe DNA modification and target DNA hybridization. Fig. 3c shows the wavelength shift with target DNA hybridization for PNDs and PNHs in air and PBS. The sensitivity of PNHs for the DNA hybridization detection of PNHs was higher than that of PNDs in both air and PBS, which agrees with the slope of the SRIS in the responsive region (Fig. S8). Thus, the SRIS in the responsive region can reflect the

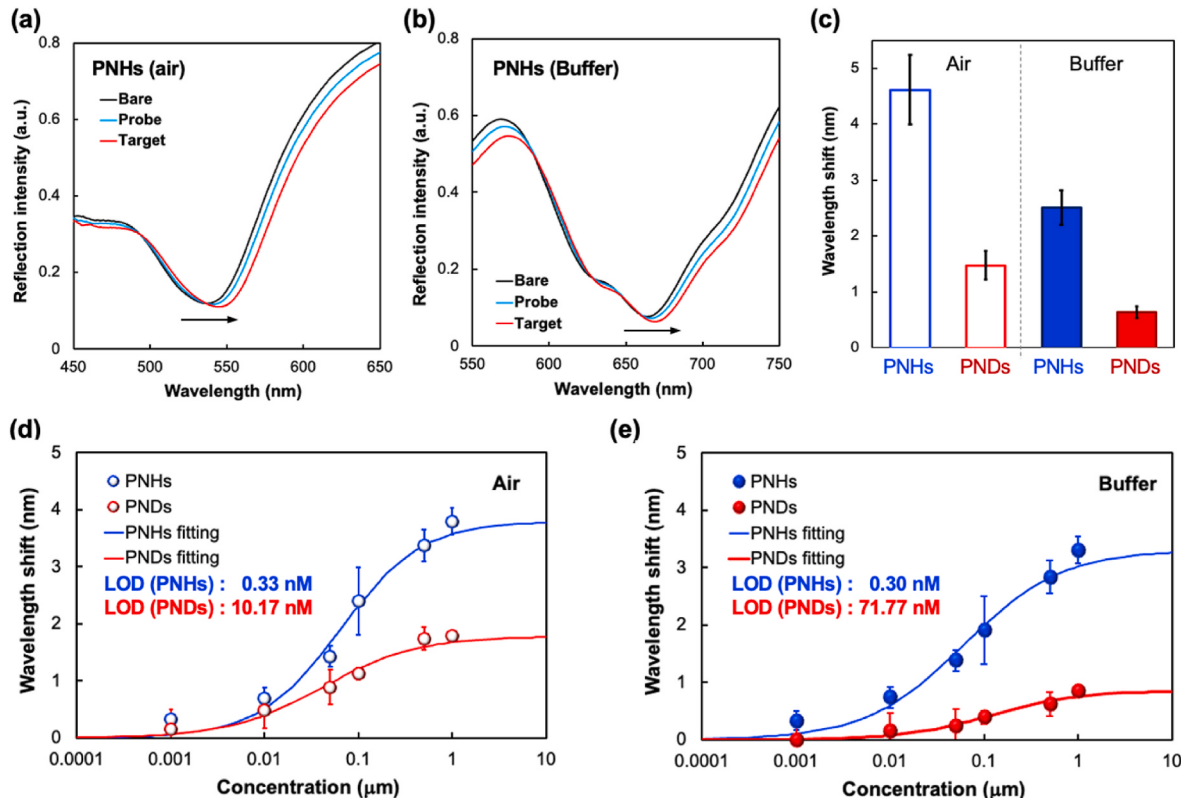


Fig. 3. Sensitivity for DNA hybridization detection. (a, b) Reflection spectra of the PNHs of bare (Black), before probe DNA immobilization (Blue), and after target DNA hybridizations (Red) in air (a) and the PBS buffer condition (b). (c) The comparison of peak wavelength shift of PNDs and PNHs with DNA hybridization under the air and buffer conditions. (d, e) Response curves of PNDs and PMHs under the air (d) and buffer conditions (e). The LODs were written in the figure. The error bars represent the standard deviation (SD) in triplicate measurements ($N = 3$).

sensitivity of label-free biomolecular detection. Fig. 3d and e shows the response curves of the PNHs and PNDs in air and PBS in the DNA concentration range of 1 nM to 1 μ M. The response curve is based on a four-parameter logistic regression equation fitted to the experimental plots (Yavas et al., 2017) (See Text S3, Table S3). According to the fitting parameters in the response curve, the limit of detections (LODs) based on 3SD value of PNDs and PNHs in air were 10.17 and 0.33 nM, respectively. The LODs of PNDs and PNHs in PBS were 71.77 and 0.30 nM, respectively. The PNHs exhibited lower LOD values under both air and water conditions because of their higher SRIS values than those of the PNDs. The wavelength resolution of the spectrometer (~ 0.2 nm in this experiment) is also responsible for the LOD values. We confirmed that our plasmonic crystal sensor could specifically detect the hybridization of target DNAs by comparing the wavelength shifts with the same concentration of mismatched DNAs, which were composed of a 40 bp sequences (Fig. S9). DNA hybridization induces a localized RI change because immobilized probe DNAs are non-uniform on the surface.

Further, DNA hybridization events differ from uniform layer coatings such as LbL. The sensitivity of plasmonic modes for localized RI changes do not always agree with BRIS and SRIS because each plasmonic mode has a uniquely enhanced electric field distribution, where biomolecules can be detected. Therefore, there is room for further investigation into the sensitivity of plasmonic crystal sensors for biomolecular detection in terms of the correspondence of their modes to responsivity.

3.4. Observation of plasmonic band shift for analyzing SRIS

For PNHs, plasmonic modes degenerated at Γ -point in response to RI change were evaluated for uniform RI change with LbL coating and localized RI change with DNAs hybridization. Plasmonic bands along the K and M wavenumbers with p- and s-polarized incidence were observed in the angle range of 20–60° using our angle-resolved reflection spectroscopic setup (Fig. S2). The ratio of the plasmonic band shift to RI change was analyzed by calculating the difference in the reflection

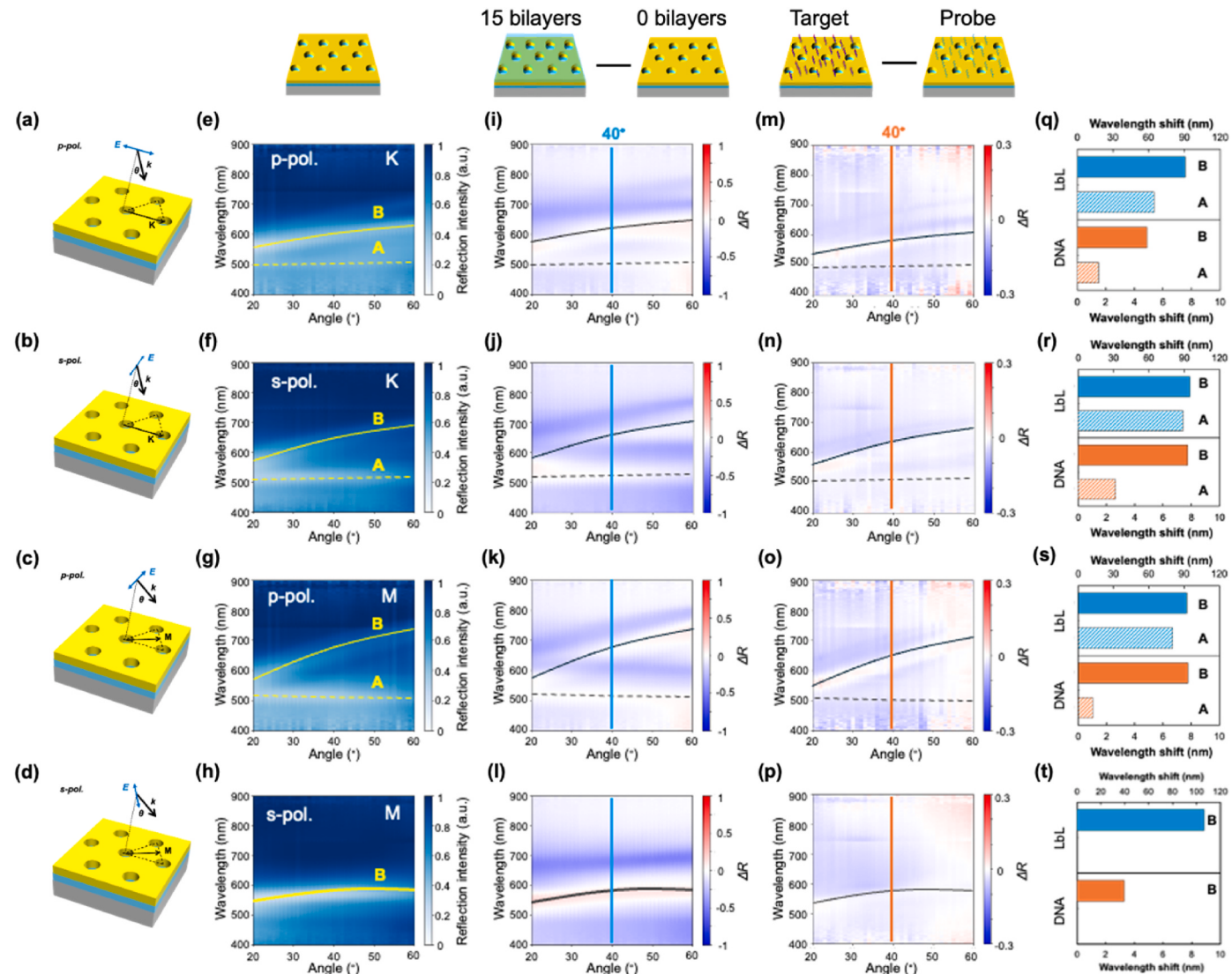


Fig. 4. Evaluation of plasmonic band shifts for RI increase. (a-d) Schematics for representing wavenumber in the reciprocal lattice, incident angle, and polarization. (e-h) Angle resolved spectrum of which the reflection intensity is shown by the blue scale in the angle range of 20–60° corresponding to the schematics in a-d. The yellow lines indicate the plasmonic bands A (dashed line) and B (solid line). (i-l) The difference of angle resolved reflection intensity from that of PNHs with 15 bilayers with LbL coating to that without LbL coating. The sky blue line indicates the reflection spectrum at an incident angle of 40°. (m-p) The difference in the angle-resolved reflection intensity from that of PNHs after to before target DNAs hybridizations with immobilized probe DNAs. The concentrations of probe and target DNAs were 1 mM. Orange line indicates the reflection spectrum at an incident angle at 40°. (q-t) The peak shifts value of modes A and B at an incident angle of 40° indicated by sky blue and orange lines in i-p. The blue and orange bars represent the shift values in the case of LbL coating and DNA hybridizations, respectively.

intensities (ΔR) at a given wavelength and incidental angle from that of PNHs after the surrounding RI increased to that of PNHs before the surrounding RI increased. Fig. 4a-d shows the incidental angles and polarization along with the corresponding wavenumbers of K or M. Fig. 4e-h represents the plasmonic bands corresponding to the schematics shown in Fig. 4a-d, respectively. Two plasmonic bands with symbols A and B can be observed in Fig. 4e-g, and only one band with the symbol B is observed in Fig. 4h. Modes A and B are considered to degenerate at the Γ -point at which the incidental angle corresponds to 0° . Modes A and B could be observed separately in the angle-resolved reflection spectrum because mode A has little dispersion with the wavenumbers compared to that of mode B. Fig. 4i-l represent the difference in reflection intensity between PNHs with 15 bilayers with and without LbL coating. Band shifts were observed along modes A and B, which were indicated by black solid and dashed lines, respectively. Fig. 4m-p shows the difference in reflection intensity between PNHs with ds-DNA and PNHs with probe DNAs, where the concentration of probe DNAs and target DNAs was $1 \mu\text{M}$. The band shifts could be observed clearly only along mode B. Fig. 4q-t shows a comparison of the wavelength shift of each mode with the LbL coating and DNA hybridization in the case of a 40° angular reflection spectrum. Mode B had a

higher sensitivity than mode A for both LbL coating and DNA hybridization; however, the difference in shift values with DNA hybridization was considerably larger than that with the LbL coating. This result suggests that mode B has a higher sensitivity to localized RI changes caused by DNA hybridization than mode A, which responds to uniform RI changes surrounding the surface.

The reflection spectra with incidental angles of 0° (Γ -point) and 40° were evaluated by experimental measurements and FDTD calculations to further investigate the sensitivity of each mode. Fig. 5 shows the results and comparison of the reflection spectra in the cases with 0° and 40° angles of p-polarized incidence along the K-direction. Fig. 5a and b shows the schematics of the incidental angle and polarization of the PNHs along the K-direction, and Fig. 5c and d represent the reflection spectra at incidental angles of 0° and 40° , respectively. The experimental spectrum at an incidental angle of 0° can be fitted by two Lorentzian curves, which can be attributed to modes A and B in Fig. 4e. These two modes are expected to degenerate at the Γ -point. FDTD calculations revealed that the electric field enhancement of mode B was considerably higher than that of mode A. The distribution of the z components of the electric field (E_z) displayed plasmonic coupling between the nanodisk and nanohole in mode B, whereas LSPs were excited

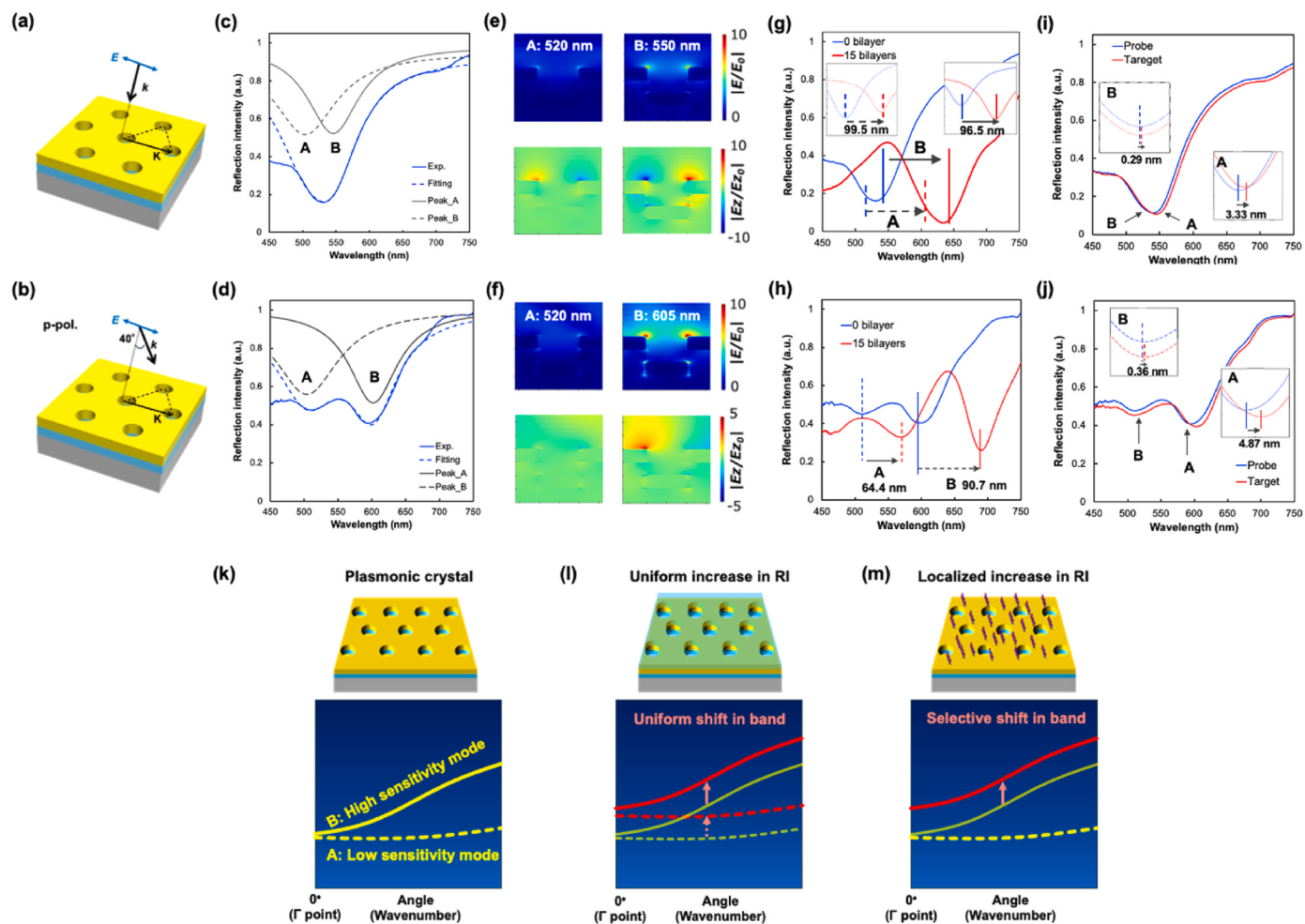


Fig. 5. Plasmonic response to uniform and localized RI change. (a, b) Schematics of incidental angle and polarization with PNHs. (c, d) Reflection spectra of PNHs at 0° (c) and 40° (d). The solid blue, dashed blue, dashed grey, and solid grey lines indicate the experimental, totally fitted, mode A-fitted, and mode B-fitted spectra, respectively. (e, f) The calculated electric field (E/E_0) and z-components (E_z/E_{z0}) distributions at a peak wavelength of mode A (left) and B (right) at an incidental angle of 0° and 40° . (g, h) The reflection spectra of PNHs without (Blue) and with (Red) LbL coating of 15 bilayers at an incidental angle of 0° and 40° . The inset represents the fitted spectrum. The peak shift values were shown with black dashed and solid arrows for peaks A and B. (i, j) The reflection spectra of PNHs without (Blue, Probe) and with (Red, Target) target DNAs at incidental angles of 0° and 40° . The inset represents the fitted spectrum. The peak shift values were shown with black dashed and solid arrows for peak A and B. (k, l, m) The schematic of the plasmonic band shift for uniform and localized RI change caused by LbL coating and DNA hybridizations.

only at the edge of the nanohole in mode A. The experimental spectrum at an incidental angle of 40° can be fitted by two Lorentzian curves, which would correspond to modes A and B. According to the fitted spectrum, mode A remained at 520 nm, whereas mode B red shifted from 550 to 605 nm, agreeing with the plasmonic band along the K-direction, as shown in Fig. 4e. In addition, the enhanced electric field distribution of mode B excited by an incidental angle of 40° was more expanded to the surrounding medium than that excited by an incidental angle of 0°, suggesting that the coupling efficiency between the plasmonic mode and incidental angle of 40° was higher than that with an incidental angle of 0°. According to the simulated reflection spectrum, mode B excited at an incidental angle of 40° showed a narrower band of higher absorption intensity than that excited at incidental angle of 0° (Fig. S11). Fig. 5g and h shows the reflection spectra of PNHs with 15 bilayers with LbL coating and those without a coating. The inset of Fig. 5g shows the fitting curves of peaks A and B, which are red shifted because of the LbL coating. For an incidental angle of 0°, approximately equal redshifts were observed for peaks A (99.6 nm) and B (96.5 nm), whereas for an incidental angle of 40°, the red shift of peak A (64.4 nm) was smaller than that of peak B (90.7 nm). These results suggest that mode B had a higher sensitivity than that of mode A in the oblique-angle incidence, although modes A and B responded to uniform RI changes surrounding the PNHs' surface. Mode A barely responded to DNA hybridization regardless of the incidental angle, 0.29 nm at 0° and 0.36 nm at 40°, whereas mode B responded more for an incidental angle of 40° (4.87 nm) than that of 0° (3.33 nm) (Fig. 5i and j). This supports the results shown in Fig. 4 that mode A had little sensitivity to localized RI changes caused by DNA hybridization, whereas the sensitivity of mode B depended on the incidental angle, which was related to the coupling efficiency between the LSP and incidence. This trend of the sensitivities of modes A and B were confirmed by the angle-resolved spectra of the other plasmonic bands (Fig. S12). Fig. 5k–m represent the schematics of the sensitivity of modes A and B to uniform and localized RI changes caused by the LbL coating and DNA hybridization. Mode A, with low sensitivity, was supported by localized plasmons on the edges of the holes depending on the plasma frequency of gold, whereas mode B, with high sensitivity, was supported by SLRs on the arrayed nanoholes coupled with nanodisks. Both modes could be shifted by a uniform RI change because of the LbL coating, whereas only mode B could be shifted by a localized RI change. Further, DNA hybridization was expected to occur on the surface of the nanoholes. This aspect related to the localized RI change was not found in the BRIS and SRIS evolutions based on a uniform RI change. In addition, more sensitive detection could be performed using the optimized angle reflection spectroscopic setup, that is, using the proper wavenumber of the SLR mode. Angle-resolved plasmonic biosensing offers a clearer observation of signals by target biomolecules because several plasmonic modes degenerate at the Γ -point and respond; however, they may have different sensitivities and offer a wider band of peaks, which is unfavorable to observe the spectral response.

4. Conclusions

The sensitivity of PNDs- and PNHs based plasmonic sensors was investigated with respect to the BRIS, SRIS, and label-free detection of DNA hybridization. The BRIS of the PNHs (447.6 nm/RIU) was approximately three times higher than that of the PNDs (142.0 nm/RIU). The PNHs had longer effective decay lengths than the PNDs under both air and water conditions. The sensitivity of the DNA hybridization detection of PNHs was higher than that of PNDs under both air and water conditions, and the sensitivity in air was higher than that in water for both PNDs and PNHs. An excellent LOD value of 0.3 nM was achieved with PNHs under both air and water conditions, which was comparable with various highly sensitive label-free DNA sensors (Bonyár, 2020). Comparing the plasmonic band shifts caused by DNA hybridization with those caused by LbL revealed that the SLR-based

mode responded much more to localized RI change than the LSP-based mode. This result suggests that the sensitivity for biomolecular detection, which is considered to cause localized RI changes, could not be completely evaluated using only the BRIS and SRIS values obtained from uniform RI change-based measurements. Moreover, more efficient coupling between oblique incidence and the SLR-based plasmonic mode could offer higher sensitivity to DNA hybridization because of the higher and wider enhancement of the electric field on the PNHs surface. Therefore, the optimized angle reflection spectroscopic setup offered a more highly sensitive label-free biosensing platform with PNHs plasmonic sensors. This study focused on the sensitivity to DNA detection which is attributed to RI change due to DNA hybridizations. We proposed the general way to evaluate and deal with plasmonic crystal biosensor. However, considering application of plasmonic crystals into another label-free biosensing like antigen detection, it should be taken into consideration that the schematics of RI change in nanoscale is different in each other. Thus, our results do not always reflect the general sensitivity of plasmonic crystal biosensor. In future, we plan to develop and perform more sensitive label-free detection and quantification of the APC sequence DNAs with a PNHs plasmonic sensor set in an angle-tunable reflection spectroscopic system, which would be compatible with biosensing experimental conditions with a flow system.

Funding

This study was supported by the Japan Society for the Promotion of Science (JSPS).

Data and material availability

All data needed to evaluate the conclusions of this study are presented in the paper and/or Supplementary Materials.

CRediT authorship contribution statement

Daiki Kawasaki: Writing – review & editing, Writing – original draft, Methodology, Investigation. **Ryosuke Nishitsuji:** Formal analysis, Data curation. **Tatsuro Endo:** Writing – review & editing, Writing – original draft, Supervision, Project administration, Investigation, Funding acquisition, Conceptualization.

Declaration of competing interest

The authors declare the following financial interests/personal relationships which may be considered as potential competing interests: Tatsuro Endo reports financial support was provided by Japan Society for the Promotion of Science. If there are other authors, they declare that they have no known competing financial interests or personal relationships that could have appeared to influence the work reported in this paper.

Data availability

Data will be made available on request.

Appendix A. Supplementary data

Supplementary data to this article can be found online at <https://doi.org/10.1016/j.bios.2024.116659>.

References

- Altug, H., Oh, S.H., Maier, S.A., Homola, J., 2022. Nat. Nanotechnol. 17, 5–16. <https://doi.org/10.1038/s41565-021-01045-5>.
- Anker, J.N., Hall, W.P., Lyandres, O., Shah, N.C., Zhao, J., Duyne, R.P. Van, 2008. Nat. Mater. 7, 8–10.

- Ansaryan, S., Liu, Y.C., Li, X., Economou, A.M., Eberhardt, C.S., Jandus, C., Altug, H., 2023. Nat. Biomed. Eng. 7, 943–958. <https://doi.org/10.1038/s41551-023-01017-1>.
- Belushkin, A., Yesilkoy, F., González-López, J.J., Ruiz-Rodríguez, J.C., Ferrer, R., Fàbrega, A., Altug, H., 2020. Small 16. <https://doi.org/10.1002/smll.201906108>.
- Bonyár, A., 2020. ACS Appl. Nano Mater. 3, 8506–8521. <https://doi.org/10.1021/acsanm.0c01457>.
- Chung, T., Lee, S., Song, E.Y., Chun, H., Lee, B., 2011. Sensors 11, 10907–10929.
- Endo, T., Ozawa, S., Okuda, N., Yanagida, Y., Tanaka, S., 2010. Sens. Actuators, B 148, 269–276.
- Endo, T., Sato, M., Kajita, H., Okuda, N., Tanaka, S., Hisamoto, H., 2012. Lab Chip 12, 1995–1999.
- Esteller, M., Corn, P.G., Baylin, S.B., Herman, J.G., 2001. Cancer Res. 61, 3225–3229.
- Feldötö, Z., Varga, I., Blomberg, E., 2010. Langmuir 26, 17048–17057. <https://doi.org/10.1021/la102351f>.
- Feuz, L., Jo, P., Jonsson, M.P., Ho, F., 2010. ACS Nano 4, 2167–2177.
- Ge, C., Fang, Z., Chen, J., Liu, J., Lu, X., Zeng, L., 2012. Analyst 137, 2032–2035. <https://doi.org/10.1039/c2an35043b>.
- Guo, L., Jackman, J.A., Yang, H., Chen, P., Cho, N., Kim, D., 2015. Nano Today 10, 213–239. <https://doi.org/10.1016/j.nantod.2015.02.007>.
- Jatschka, J., Dathe, A., Csáki, A., Fritzsche, W., Stranik, O., 2016. Sens. Bio-Sens. Res. 7, 62–70.
- Kawasaki, D., Maeno, K., Yamada, H., Sueyoshi, K., Hisamoto, H., Endo, T., 2019a. Sensor. Actuator. B Chem. 299, 126932 <https://doi.org/10.1016/j.snb.2019.126932>.
- Kawasaki, D., Yamada, H., Maeno, K., Sueyoshi, K., Hisamoto, H., Endo, T., 2019b. ACS Appl. Nano Mater. 2, 4983–4990. <https://doi.org/10.1021/acsnano.9b00930>.
- Kawasaki, D., Yamada, H., Sueyoshi, K., Hisamoto, H., Endo, T., 2022. Biosensors 12. <https://doi.org/10.3390/bios12040200>.
- Kim, D., Kerman, K., Saito, M., Sathuluri, R.R., Endo, T., Yamamura, S., Kwon, Y., Tamiya, E., 2007. Anal. Chem. 79, 1855–1864.
- Kravets, V.G., Kabashin, A.V., Barnes, W.L., Grigorenko, A.N., 2018. Chem. Rev. 118, 5912–5951. <https://doi.org/10.1021/acs.chemrev.8b00243>.
- Li, F., Shen, J., Guan, C., Xie, Y., Wang, Z., Lin, S., Chen, J., Zhu, J., 2022. Biosens. Bioelectron. 203, 114038 <https://doi.org/10.1016/j.bios.2022.114038>.
- Li, X., Soler, M., Özdemir, C.I., Belushkin, A., Yesilköy, F., Altug, H., 2017. Lab Chip 17, 2208–2217. <https://doi.org/10.1039/c7lc00277g>.
- Luo, X., Xing, Y., Galvan, D.D., Zheng, E., Wu, P., Cai, C., Yu, Q., 2019. ACS Sens. 4, 1534–1542. <https://doi.org/10.1021/acssensors.9b00008>.
- Nishiguchi, K., Sueyoshi, K., Hisamoto, H., Endo, T., 2016. Jpn. J. Appl. Phys. 55.
- Ray, K., Badugu, R., Lakowicz, J.R., 2007. Chem. Mater. 19, 5902–5909. <https://doi.org/10.1021/cm071510w>.
- Sadighbayan, D., Hasanzadeh, M., Ghafar-Zadeh, E., 2020. TrAC - Trends Anal. Chem. 133, 116067 <https://doi.org/10.1016/j.trac.2020.116067>.
- Shrivastav, A.M., Cvelbar, U., Abdulhalim, I., 2021. Commun. Biol. 4, 1–12. <https://doi.org/10.1038/s42003-020-01615-8>.
- Sreekanth, K.V., Alapan, Y., ElKabbash, M., Ilker, E., Hinczewski, M., Gurkan, U.A., De Luca, A., Strangi, G., 2016. Nat. Mater. 15, 621.
- Szunerits, S., Boukherroub, R., 2012. Chem. Commun. 48, 8999–9010.
- Tang, L., Li, J., 2017. ACS Sens. 2, 857–875. <https://doi.org/10.1021/acssensors.7b00282>.
- Willets, K.A., Duyne, R.P. Van, 2007. Annu. Rev. Phys. Chem. 58, 267–297.
- Yavas, O., Svedendahl, M., Dobosz, P., Sanz, V., Quidant, R., 2017. Nano Lett. 17, 4421–4426. <https://doi.org/10.1021/acs.nanolett.7b01518>.
- Zhan, C., Liu, B.W., Liu, B.W., Tian, Z.Q., Ren, B., 2020. J. Am. Chem. Soc. 142, 10905–10909. <https://doi.org/10.1021/jacs.0c01907>.